SUPPLEMENTAL MATERIAL

In the following we provide additional details regarding several aspects of the experiment and associated theoretical investigation. We begin with a discussion of the techniques used to produce the resonators and the embedded CPTs, and of how important CPT parameters such as charging and Josephson energies are determined. We then discuss the two biasing schemes used to produce the experimental results in the manuscript. One biasing scheme was used for low-noise current measurements, while the other was used to produce highly stable emission for spectral measurements. Next, we turn to the techniques used for measuring cavity emission, and for characterization and modeling of the system amplifier noise. Finally, we give a more in-depth analysis of our theoretical model of the system.

Sample Fabrication and Characterization

The cavities used for fabricating our cCPTs were based on coplanar waveguide with inductively terminated dc bias lines attached to the main cavity line a distance $\lambda/4$ from the ends of the cavity, as described in detail elsewhere.[1] The Nb film of the cavity was 100 nm thick and was etched with sloping side walls to allow for good step coverage during deposition of the CPT. Oxide was removed under the Au/Ti contact pads by ion milling before deposition of the metal. A micrograph of a typical cavity is shown in Fig. S1a.

The central cavity conductor was 10 μm wide with 5.5 μm gaps between the central conductor and ground. Capacitive coupling to the cavity was strongly asymmetric, with a small (1.7 fF) input capacitor and a large (18.5 fF) output capacitor (right inset, Fig. S1a). The inductors on the dc bias lines (left inset, Fig. S1a) were large enough (5.8 nH) that few photons escape from the cavity through the bias circuitry. Overall, we estimate that roughly 95% of the cavity photons are collected by the microwave circuitry for amplification and subsequent analysis. The measured cavity Q of 3500 is in good agreement with the simulated Q (including the dc bias lines) of 3600. The measured cavity resonant frequency of $\omega_0 = 5.256$ GHz was in similarly good agreement with the design resonant frequency of 5.4 GHz.

The CPT itself was fabricated in a separate step using standard electron beam lithography and shadow evaporation techniques,[2] and aligned with the cavity so as to lie in the gap between the central conductor and ground planes as shown schematically in Fig. S1b. The leads of the CPT were thick enough (70 nm) to drive the underlying Au/Ti contact pads in Fig. S1c superconducting by means of the proximity effect. The CPT island, on the other hand, was very thin (7 nm), and deposited using a cooled evaporation stage to ensure electrical continuity.

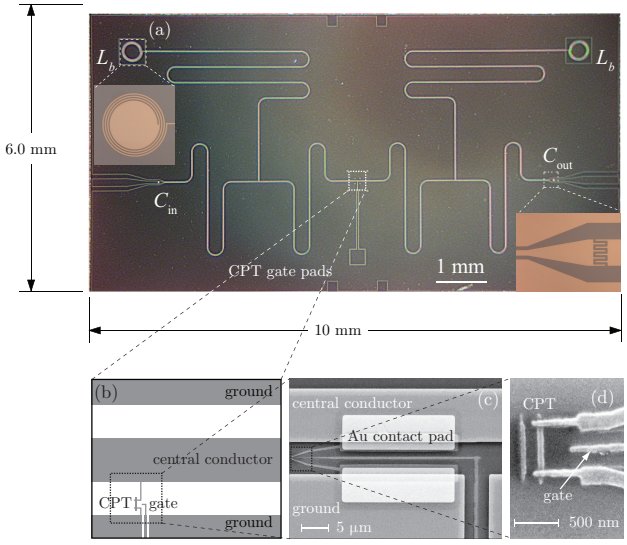

FIG. S1. **Sample design. a,** Optical micrograph of a dc-biased cavity showing the location of the CPT and typical designs for an output capacitor and dc bias line inductor. **b,** Schematic illustration of the location of the CPT relative to the cavity. **c,** Electron micrograph of the coupling between the CPT and the contact pads. **d,** Electron micrograph of a typical CPT.

This technique increases the superconducting gap of the CPT island, preventing quasiparticle trapping and ensuring $2e$-periodicity of the CPT I-V characteristics and photon emission patterns.[3]

Three separate cCPT samples were fabricated in the course of this experiment. Of these, microwave measurements of cavity output were performed on two. All three samples showed similar behavior in their I-V characteristics, with all major features described in the main text clearly visible. Both samples for which microwave measurements were performed showed microwave photon emission at the first two cotunneling features. The detailed dc and microwave measurements presented in the main text were all obtained from a single sample.

The junction and gate capacitances for the sample were determined from the dc transport data. The $2e$ periodicity of the supercurrent determines the gate capacitance $C_g = 4.6$ aF. The junction capacitances are determined by fitting to the sequential tunneling plus photon emission features described in the main text, giving a source capacitance $C_S = 1.08$ fF and a drain capacitance $C_D = 1.14$ fF. The resulting total capacitance $C_\Sigma = C_S + C_D + C_g = 2.22$ fF gives a charging energy $E_c = e^2/2C_\Sigma = 36\ \mu$eV $= 0.42$ K. The Josephson energy E_J was determined from the total normal-state CPT tunneling resistance $R_n = 21.5\ \text{k}\Omega$ through the Ambegaokar-Baratoff relation $E_J = \Delta\frac{R_Q}{R_n}$, giving $E_J \approx 64\ \mu$eV $= 0.74$ K. Here $\Delta = 212\ \mu$eV is the effective superconducting gap when the different gap

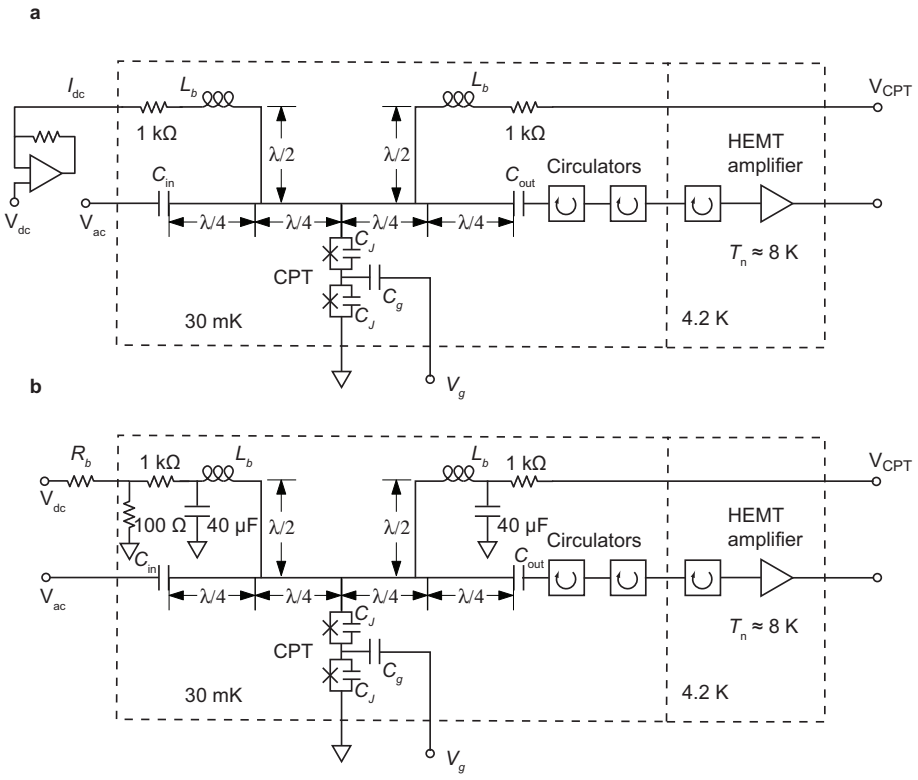

FIG. S2. **DC and microwave circuitry. a,** Circuit for low-noise current measurements using a floated current sensitive amplifier. Detection of microwave signals is possible with this setup but emission is not stable. **b,** Circuit for stable microwave emission measurements. The use of a cold voltage divider and a large capacitor provide excellent bias stability but limit resolution in measurements of current.

sizes of the leads and island are taken into account, and $R_Q = h/4e^2 \approx 6.45\,\mathrm{k\Omega}$ is the resistance quantum.[3]

All electrical measurements were performed in a dilution refrigerator at its base temperature of 30 mK. The dc bias lines were filtered with room temperature RC and π-type filters, as well as cryogenic copper powder microwave filters. The sample was mounted in a sealed gold-plated Cu box designed to minimize propagation of unwanted microwave modes. The box was in turn located inside a cryogenic Amumetal magnetic shield to minimize the residual magnetic field at the sample location.

dc Biasing Schemes

We used two separate dc biasing schemes during the experiment, as shown in Fig. S2. One scheme is optimized for sensitive measurements of current and was used for the I-V measurements shown in the main text. The other is optimized for low voltage noise on the bias line and is used for emission measurements.

In Fig. S2(a) we show our standard circuitry for low-noise current measurements. Cold 1 kΩ resistors on the dc bias lines are used to help protect the cCPT from electrostatic discharge. On the ac input side of the cavity, multiple cold attenuators (total 50 dB, not shown) are used to prevent noise from entering the cavity. On the output side, three circulators are interposed between the cavity and the cryogenic HEMT amplifier to prevent the noise wave at the amplifier input from entering the cavity. After the HEMT amplifier, additional room temperature amplification is performed on the signal before further measurement.

Since the cCPT is grounded internally in the dilution refrigerator, the current sensitive amplifier is floated and the dc bias voltage V_{dc} is applied indirectly to the cCPT through the amplifier. This provides current resolution on the order of a few fA, allowing the highly detailed I-V measurements shown in the main text. Voltage resolution was limited to roughly $\pm 1\ \mu$V by the noise of the voltage amplifier. An additional example of an I-V characteristic taken using this method is shown in Fig. S3; this measurement, taken from positive bias toward negative bias, was made with greater voltage resolution than the I-V characteristics shown in Fig. 2(b) in the main text. It shows hysteresis and discontinuities in the voltage V_{CPT} across the CPT similar those in Fig. 2(b), but with greater detail.

Emission stability is limited when using the measure-

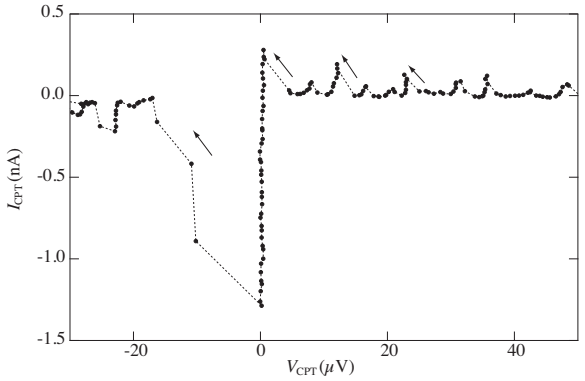

FIG. S3. Detailed I-V characteristic for the cCPT at a gate voltage far removed from charge degeneracy, sweeping from positive to negative bias, as indicated.

ment circuitry in Fig. S2a for two reasons. First, noise associated with the room temperature bias circuitry can cause significant fluctuations in the drive voltage, leading to fluctuations in the drive frequency ω_J. These can be only partially eliminated by use of low-pass filtering at room temperature.

Further improvement can be made as in Fig. S2b by adding a cryogenic 100 Ω resistor in parallel with the 1 kΩ protective resistor and sample. In combination with a room temperature biasing resistor $R_b \approx 100$ kΩ the 100Ω resistor forms a cold voltage divider that drastically reduces the amplitude of low-frequency noise reaching the sample.

More fundamentally, however, we must also consider the thermal noise associated with the cold 1 kΩ protective resistors; this noise is not negligible despite the resistor's low temperature. For instance, assume that thermal noise in a bandwidth $B \approx 1$ MHz from the $R = 1$ kΩ resistors can reach the sample. The associated rms noise voltage $V_n = \sqrt{4k_BT(2R)B} = 60$ nV at $T = 30$ mK, when applied to the cCPT, results in a drive frequency jitter $\delta\omega_J = 2\pi \times 2eV_n/h \approx 30$ MHz that is far larger than the cavity bandwidth $\kappa = 2\pi \times 1.5$ MHz.

This noise can be significantly reduced, however, by placing a large cryogenic capacitor $C \approx 40$ μF between the 1 kΩ resistor and the cCPT. The resulting noise reaching the cCPT can be estimated as $V_n = \sqrt{2k_BT/C} \approx 0.14$ nV. The drive frequency jitter is then drastically reduced to $\delta\omega_J \approx 2\pi \times 35$ kHz, on the order of the sharpest spectral features we measure. This vastly improved bias stability has made possible the highly detailed emission measurements presented in the main text.

Determination of V_{CPT} from n_{ph}

The CPT voltage V_{CPT} was monitored during the very slow sweeps with closely spaced values of V_{dc} used to produce the spectra in Figs. 2, 3 and 4 in the main text. However, the ±1 μV peak-to-peak voltage noise added by our amplifier made the V_{CPT} data far too noisy to be useful in plotting false-color images, and of limited use in plotting n_{ph}. Also, our reduced current sensitivity during the high-stability measurements made direct measurement of I_{CPT} impossible.

To circumvent these difficulties for the biasing scheme shown in Fig. S2(b), we chose to estimate V_{CPT} and I_{CPT} from the microwave data, which is far cleaner. We make the physically reasonable assumption that all the energy injected into the CPT appears as photons in the resonator, so that

$$I_{\mathrm{CPT}}V_{\mathrm{CPT}} = \kappa\hbar\omega_0 n_{\mathrm{ph}}$$

where κ is the decay rate of the cavity, ω_0 is the resonant frequency, and n_{ph} is the number of photons. This assumption is supported experimentally by the good agreement between the measured total power $I_{\mathrm{CPT}}V_{\mathrm{CPT}}$ dissipated in the CPT (determined using high current sensitivity biasing) and the measured microwave output power. We further assume that the applied voltage V_{dc} is related to V_{CPT} and I_{CPT} by Kirchoff's law

$$V_{\mathrm{dc}} = V_{\mathrm{CPT}} + I_{\mathrm{CPT}}R_s$$

where $R_s \approx 1.1$ kΩ is the effective source resistance of the bias voltage. Solving these equations for V_{CPT} and I_{CPT} gives

$$V_{\mathrm{CPT}} = \frac{V_{\mathrm{dc}} + \sqrt{V_{\mathrm{dc}}^2 - 4\kappa\hbar\omega_0 n_{\mathrm{ph}}R_s}}{2},$$

and

$$I_{\mathrm{CPT}} = \frac{\kappa\hbar\omega_0 n_{\mathrm{ph}}}{V_{\mathrm{CPT}}}.$$

Since typically $4\kappa\hbar\omega_0 n_{\mathrm{ph}}R_s \ll V_{\mathrm{dc}}^2$, the corrections to V_{CPT} tend to be on the order of a few percent of V_{dc}.

In order to calibrate V_{dc}, we make use of the fact that during a ramp of the bias voltage, V_{dc} is given by

$$V_{\mathrm{dc}} = V_0 + \delta V N$$

for the Nth point in the ramp. Here δV is a well-known small voltage increment and V_0 is a voltage offset that is known to be $V_0 \approx 9 \pm 2$ μV for the first peak and $V_0 \approx 20 \pm 2$ μV for the second.

To set the value of V_0 for plotting purposes, we choose V_0 so that $V_{\mathrm{CPT}} = \hbar\omega_0/2e = 10.9$ μV at maximum emission for the first peak and $V_{\mathrm{CPT}} = (2\hbar\omega_0)/2e = 21.8$ μV for the second peak. Setting V_0 to different values within its range of uncertainty only results in a lateral shift in plots of I_{CPT} or n_{ph} versus V_{CPT} without any significant change in shape.

Microwave Measurements

After exiting the cavity, microwave photons pass through three circulators and then enter the amplifier chain, which consists of a cryogenic HEMT amplifier with noise temperature $T_n = 8$K and gain $G_1 = 38$dB followed by a bandpass filter and then a room temperature FET amplifier with gain $G_2 = 45$ dB.

We can use the shot noise of the CPT itself, when driven on its quasiparticle branch, to fully calibrate the amplifier chain. This is essentially the same technique long used to calibrate system gain and noise for the related RF-SET.[4] A straightforward calculation shows that the shot noise power $P_{\rm SN}$ delivered by the cCPT to the HEMT amplifier is given by

$$P_{\rm SN} = \frac{eI}{4\mathcal{C}}\frac{Q_e}{Q_c} \tag{S1}$$

where I is the driving current and $\mathcal{C}$ is the total cavity capacitance. The cavity Q is written here as Q_c, while Q_e is the cavity Q when additionally loaded by the CPT high bias tunneling resistance R_n, given by $Q_e^{-1} = Q_c^{-1} + Q_{\rm CPT}^{-1}$ where $Q_{\rm CPT} = \omega_0 R_n \mathcal{C}$. As can be seen in Fig. S4a, the measured shot noise power clearly scales linearly with the applied driving current. From (S1), the slope of the measured power $P_{\rm SN}$ versus I in Fig. S4a is given by $eGQ_e/4\mathcal{C}Q_c$ where G is the gain of the amplifier chain. The y intercept P_0 of the linear fits for positive and negative I give the system noise temperature via the relation $T_n = P_0/k_B G\,\mathrm{BW}$ where BW = 20 MHz is the bandwidth of the measurement. The data in Fig. S4a give a system gain of 68 dB at the output of the FET amplifier and a system noise temperature $T_n = 31$ K.

To determine the number of cavity photons $n_{\rm ph}$ from the emission spectra $S(\omega)$, we simply integrated each spectrum and subtracted the measured amplifier noise from the result to obtain a measurement of the total microwave power $P_{\rm CPT}$ emitted by the CPT for a given set of bias conditions. The cavity occupation is then determined from $P_{\rm CPT}$ by the relation $n_{\rm ph} = P_{\rm CPT}/\kappa\hbar\omega_0$.

Derivation of the CCPT Hamiltonian

In this section, we derive the cCPT Hamiltonian (1), starting with a simplified 1D model of the cCPT system shown in Fig. S5. While such a model does not yield the actual mode spectrum, it does serve as a useful 'scaffold' for deriving the approximate discrete mode equations and associated lumped element model, where the element parameters (i.e., capacitances, inductances etc.) can be selected so that the resonant mode frequencies and coupling strengths accurately match the experimentally determined ones. Referring to the circuit in Fig. S5, Kirchhoff's laws yield the following equations in terms of

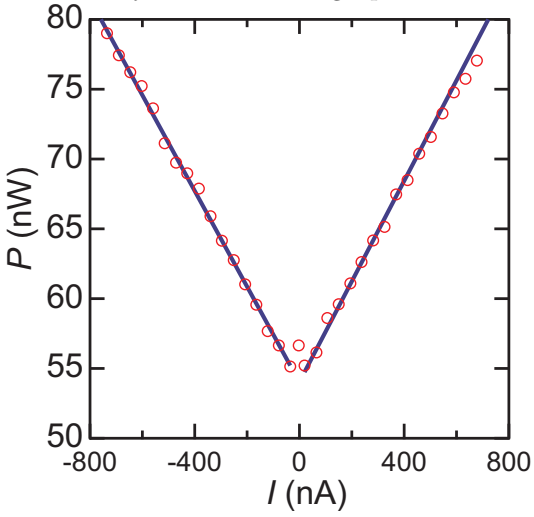

FIG. S4. **Amplifier chain noise characterization.** Noise power emitted by the cCPT in its bandwidth κ (red circles) versus driving current I. The slope of the blue fitted lines gives the total system gain, while their intercept gives the system noise temperature.

the CPT phases $\gamma_\pm(t) = (\varphi_1(t) \pm \varphi_2(t))/2$ (with φ_1, φ_2 the gauge invariant phases across the Josephson junctions), the cavity phase field $\phi_c(x,t)$, and transmission line phase field $\phi_T(x,t)$:

$$2C_J\frac{\Phi_0}{2\pi}\frac{d^2\gamma_+}{dt^2} + 2I_c\sin\gamma_+\cos\gamma_- - C_g\frac{dV_g}{dt} = \frac{\Phi_0}{\pi\mathcal{L}_c}\left(\left.\frac{\partial\phi_c}{\partial x}\right|_{x=0^+} - \left.\frac{\partial\phi_c}{\partial x}\right|_{x=0^-}\right), \tag{S2}$$

$$2C_J\frac{\Phi_0}{2\pi}\frac{d^2\gamma_-}{dt^2} + 2I_c\cos\gamma_+\sin\gamma_- + C_g\frac{dV_g}{dt} = 0, \tag{S3}$$

$$\frac{\partial^2\phi_c}{\partial t^2} = (\mathcal{L}_c\mathcal{C}_c)^{-1}\frac{\partial^2\phi_c}{\partial x^2},\ -L/2 < x < 0;\ 0 < x < L/2, \tag{S4}$$

$$\frac{\partial^2\phi_T}{\partial t^2} = (\mathcal{L}_T\mathcal{C}_T)^{-1}\frac{\partial^2\phi_T}{\partial x^2},\ x < -L/2;\ L/2 < x, \tag{S5}$$

and junction conditions

$$2\frac{d\gamma_+}{dt} = \left.\frac{\partial\phi_c}{\partial t}\right|_{x=0}, \tag{S6}$$

$$\phi_c(L/4,t) - \frac{L_b}{\mathcal{L}_c}\left(\left.\frac{\partial\phi_c}{\partial x}\right|_{x=L^+/4} - \left.\frac{\partial\phi_c}{\partial x}\right|_{x=L^-/4}\right) = \frac{2\pi}{\Phi_0}V_{\rm dc}t, \tag{S7}$$

$$\begin{aligned} -\frac{1}{\mathcal{L}_c}\left.\frac{\partial\phi_c}{\partial x}\right|_{x=L^-/2} &= C\left(\frac{\partial^2\phi_c}{\partial t^2} - \frac{\partial^2\phi_T}{\partial t^2}\right)\Big|_{x=L/2}, \\ -\frac{1}{\mathcal{L}_T}\left.\frac{\partial\phi_T}{\partial x}\right|_{x=L^+/2} &= C\left(\frac{\partial^2\phi_c}{\partial t^2} - \frac{\partial^2\phi_T}{\partial t^2}\right)\Big|_{x=L/2}, \end{aligned} \tag{S8}$$

$$\begin{aligned} -\frac{1}{\mathcal{L}_c}\left.\frac{\partial\phi_c}{\partial x}\right|_{x=-L^+/2} &= C\left(\frac{\partial^2\phi_T}{\partial t^2} - \frac{\partial^2\phi_c}{\partial t^2}\right)\Big|_{x=-L/2}, \\ -\frac{1}{\mathcal{L}_T}\left.\frac{\partial\phi_T}{\partial x}\right|_{x=-L^-/2} &= C\left(\frac{\partial^2\phi_T}{\partial t^2} - \frac{\partial^2\phi_c}{\partial t^2}\right)\Big|_{x=-L/2}, \end{aligned} \tag{S9}$$

where the phase fields and their time derivatives are continuous across the junctions, and we assume $C_J \gg C_g$. We shall work in terms of the shifted cavity field: $\tilde{\phi}_c = \phi_c - \frac{2\pi}{\Phi_0}V_{\rm dc}t$, so that Eq. (S7) becomes

$$\phi_c(L/4,t) - \frac{L_b}{\mathcal{L}_c}\left(\left.\frac{\partial\phi_c}{\partial x}\right|_{x=L^+/4} - \left.\frac{\partial\phi_c}{\partial x}\right|_{x=L^-/4}\right) = 0 \tag{S10}$$

and Eq. (S6) becomes

$$\gamma_+(t) = (\phi_c(0,t) + \omega_J t)/2, \tag{S11}$$

where the driving frequency is $\omega_J = 2\pi V_{\rm dc}/\Phi_0 = 2eV_{\rm dc}/\hbar$ and we have dropped the tilde on ϕ_c for notational convenience. Note that we make no distinction between $V_{\rm dc}$ and $V_{\rm CPT}$ in our model as we consider a simplified system in which the additional impedance on the bias line, Z_b, is neglected. We can now use Eq. (S11) to eliminate γ_+ from the dynamical equations; Eqs. (S3) and (S2) become respectively

$$2C_J\frac{\Phi_0}{2\pi}\frac{d^2\gamma_-}{dt^2} + 2I_c\cos\left[(\phi_c(0,t)+\omega_J t)/2\right]\sin\gamma_- + C_g\frac{dV_g}{dt} = 0 \tag{S12}$$

and

$$\phi_c'(0,t) - \frac{C_J}{4\mathcal{C}_c}\phi_c''(0,t) = \frac{\pi\mathcal{L}_c I_c}{\Phi_0}\sin\left[(\phi_c(0,t)+\omega_J t)/2\right]\cos\gamma_- - \frac{\pi\mathcal{L}_c}{2\Phi_0}C_g\dot{V}_g, \tag{S13}$$

where we have used the cavity wave equation to replace $\ddot{\phi}_c$ with ϕ_c'', and have also used $\phi_c'(0^+,t) = -\phi_c'(0^-,t)$ a consequence of the fact that only the symmetric about the origin component of the phase field $\phi_c(x,t)$ (i.e., voltage antinode/current node) couples to the CPT, assuming idealized perfect symmetry of the device, with the '+' superscript on the 0 in $\phi_c'(0,t)$ dropped for notational convenience. With this symmetry consideration, the original length L cavity with the CPT situated at the midpoint is effectively replaced with a length $L/2$ cavity and where the interaction with the CPT is expressed by Eq. (S13), which can be interpreted as a (rather nontrivial) boundary condition on the cavity field $\phi_c(x,t)$ at the $x = 0$ end.

From now on, we set the cavity-transmission line coupling capacitance $C = 0$, deriving the closed cCPT system dynamics only, described by the $\phi_c(x,t)$ cavity wave equation (S4) for $0 < x < L/2$, the coupled $\gamma_-(t)$ equation (S12), the junction condition (S10) at $x = L/4$, the boundary condition (S13) at $x = 0$, and the boundary

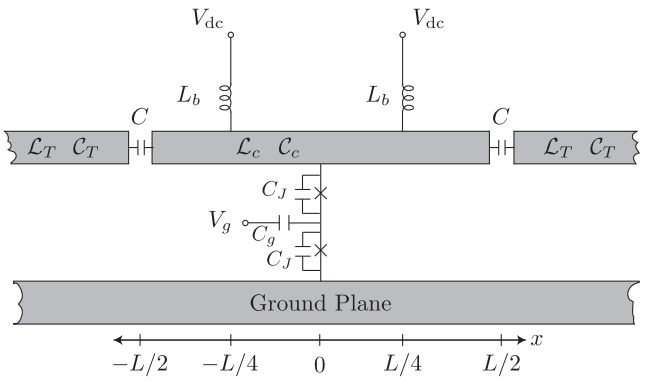

FIG. S5. Simplified model of the cavity-CPT system, where the cavity center conductor has length L, and the Josephson junctions are assumed to have equal capacitances C_J and critical currents I_c. The cavity inductance and capacitance per unit length are denoted $\mathcal{L}_c$, $\mathcal{C}_c$, respectively, while $\mathcal{L}_T$, $\mathcal{C}_T$ are the respective transmission line inductance and capacitance per unit length. The cavity and transmission line couple weakly via capacitance C. The dc bias lines involve inductances L_b.

condition

$$\left.\frac{\partial\phi_c}{\partial x}\right|_{x=L/2} = 0 \tag{S14}$$

at $x = L/2$. We solve these equations using the approximate eigenfunction expansion method, with Eq. (S13) replaced by the following simpler boundary condition at $x = 0$:

$$\phi_c'(0,t) - \frac{C_J}{4\mathcal{C}_c}\phi_c''(0,t) \approx \phi_c'(x,t)|_{x=-C_J/(4\mathcal{C}_c)} = 0, \tag{S15}$$

expressed approximately as a Neumann boundary condition evaluated at the slightly shifted endpoint $x = -C_J/(4\mathcal{C}_c)$, with $C_J/(\mathcal{C}_c L) \ll 1$.

We can now apply the method of separation of variables to the cavity wave equation (S4) for $0 < x < L/2$: the homogeneous boundary conditions (S14), (S15) and junction condition (S10) define a Sturm-Liouville problem. Taking advantage of the smallness of the capacitance ratio $C_J/(\mathcal{C}_c L)$, as well as the smallness of the inductance ratio, $\mathcal{L}_c L/L_b \ll 1$, the orthogonal eigenfunctions are approximately

$$\phi_n(x) = \begin{cases} \cos\left[k_n\left(x + C_J/(4\mathcal{C}_c)\right)\right] & \text{if } 0 < x < L/4; \\ \frac{\cos[k_n(L/4+C_J/(4\mathcal{C}_c))]}{\cos(k_n L/4)}\cos\left[k_n\left(x - L/2\right)\right] & \text{if } L/4 < x < L/2, \end{cases} \tag{S16}$$

the approximate associated wavenumber eigenvalues are

$$k_n = \frac{2\pi n}{L} - \frac{4\pi n}{L}\left(\frac{C_J}{4\mathcal{C}_c L}\right) + \begin{cases} 0 & \text{if } n \text{ odd}; \\ \frac{1}{\pi n}\frac{\mathcal{L}_c}{L_b} & \text{if } n \text{ even}, \end{cases} \tag{S17}$$

and the orthogonality condition on the eigenfunctions is approximately

$$\int_{-C_J/(4\mathcal{C}_c)}^{L/2} dx\ \phi_n(x)\phi_m(x) = 0,\ m \neq n. \tag{S18}$$

From Eqs. (S16) and (S17), we see that the odd eigenfunctions have a voltage node at approximately $x = L/4$, while from Eq. (S10), the ratio of the ac current entering the cavity through the bias line to the average ac current flowing along the cavity center conductor at $x = L/4$ is of order $(\mathcal{L}_c L/L_b)(C_J/\mathcal{C}_c L)$, i.e., second order in smallness. On the other hand, the even eigenfunctions have a voltage antinode at approximately $x = L/4$ and the ratio of the entering ac bias current to the average ac cavity current flow is of order $(\mathcal{L}_c L/L_b)(\mathcal{C}_c L/C_J) \sim 1$. Thus, wave solutions involving odd eigenfunctions are expected to have low loss, while even eigenfunction wave solutions are expected to be lossy due to the presence of the bias line.

We now assume that solutions $\phi_c(x,t)$ to the wave equation (S4) for $0 < x < L/2$ with the full boundary conditions (S13) and (S14) at $x = 0$ and $x = L/2$, respectively, can be expressed as a series expansion in terms of the eigenfunctions $\phi_n(x)$:

$$\phi_c(x,t) = \sum_n q_n(t)\phi_n(x). \tag{S19}$$

We shall assume that this series expansion can be restricted to only the odd integer eigenfunctions, with the even integer components simply accounted for through their possible effect of additional damping on the former. From Eq. (S19) and the orthogonality condition (S18), the to be determined time-dependent coefficients $q_n(t)$ (for odd n) are given as

$$q_n(t) = \frac{4}{L}\int_{-C_J/(4\mathcal{C}_c)}^{L/2} dx\ \phi_c(x,t)\phi_n(x), \tag{S20}$$

where the prefactor is the approximate normalization constant [neglecting $C_J/\mathcal{C}_c$ corrections]. Differentiating (S20) twice with respect to time and applying the cavity wave equation (S4), we have:

$$\ddot{q}_n(t) = \frac{4}{\mathcal{L}_c\mathcal{C}_c L}\int_{-C_J/(4\mathcal{C}_c)}^{L/2} dx\ \phi_c''(x,t)\phi_n(x). \tag{S21}$$

Integrating (S21) by parts twice and applying the eigenvalue equation $\phi_n''(x) = -k_n^2\phi_n(x)$ and also Eq. (S20), we obtain

$$\ddot{q}_n(t) = -\frac{k_n^2}{\mathcal{L}_c\mathcal{C}_c}q_n(t) + \frac{4}{\mathcal{L}_c\mathcal{C}_c L}\phi_c'(x,t)\phi_n(x)\Big|_{-C_J/(4\mathcal{C}_c)}^{L/2}. \tag{S22}$$

Using the boundary conditions (S13) and (S14), Eq. (S22) becomes

$$\ddot{q}_n(t) = -\omega_n^2 q_n(t) - \frac{4\pi I_c}{\Phi_0\mathcal{C}_c L}\sin\left[\frac{1}{2}\left(\sum_{n'} q_{n'}(t) + \omega_J t\right)\right]\cos\gamma_- + \frac{2\pi C_g\dot{V}_g}{\Phi_0\mathcal{C}_c L}, \tag{S23}$$

where the free cavity mode oscillator frequencies are

$$\omega_n^2 = \frac{k_n^2}{\mathcal{L}_c\mathcal{C}_c}, \tag{S24}$$

with $k_n = 2\pi n/L$, n odd. In terms of the cavity mode phase coordinates $q_n(t)$, the γ_- equation (S12) becomes

$$2C_J\frac{\Phi_0}{2\pi}\frac{d^2\gamma_-}{dt^2} + 2I_c\cos\left[\frac{1}{2}\left(\sum_n q_n(t) + \omega_J t\right)\right]\sin\gamma_- + C_g\frac{dV_g}{dt} = 0. \tag{S25}$$

Equations (S23) and (S25) give the approximate discrete mode description of the closed cCPT system dynamics. In modeling the experiment, the various circuit parameters appearing in (S23) and (S25) can be selected so as to provide the best fit to the data. In this way, the effective discrete mode equations are assumed to be more versatile than the original starting equations at the beginning of this section, which are tied to a particular model of the cavity geometry. Figure S6 shows a lumped element circuit model that yields the above discrete mode equations (neglecting small capacitance ratio terms), where the lumped capacitance and inductance elements are $C_n = \mathcal{C}_c L/2$, $L_n = 1/(\omega_n^2 C_n)$, respectively, and dissipative effective resistance elements R_n have also been included for completeness.

The closed system equations of motion (S23) and (S25) follow from the Hamiltonian

$$\begin{aligned}\mathcal{H} = &\left(\frac{2\pi}{\Phi_0}\right)^2\sum_n\frac{1}{2C_n}\left(p_n + \frac{\Phi_0}{4\pi}C_g V_g\right)^2 + \left(\frac{\Phi_0}{2\pi}\right)^2\sum_n\frac{q_n^2}{2L_n}\\ &+4E_c(N - n_g/2)^2 - 2E_J\cos\left[\frac{1}{2}\left(\sum_n q_n + \omega_J t\right)\right]\cos\gamma_-,\end{aligned} \tag{S26}$$

where the mode sums are restricted to odd n, $N = p_-/\hbar$ is minus the number of excess Cooper pairs on the island, $n_g = C_g V_g/e$ is the polarization charge induced by the applied gate voltage bias V_g, $E_c = e^2/(2C_J)$ is the approximate CPT charging energy (neglecting C_g), and $E_J = I_c\Phi_0/(2\pi)$ is the Josephson energy of a single JJ.

The quantum Hamiltonian corresponding to Eq. (S26) can be written as

$$\begin{aligned}H = &\sum_n\hbar\omega_n a_n^\dagger a_n + 4E_c\sum_{N=-\infty}^{+\infty}(N - n_g/2)^2\,|N\rangle\langle N|\\ &-E_J\sum_{N=-\infty}^{+\infty}(|N+1\rangle\langle N| + |N-1\rangle\langle N|)\cos\left[\sum_n\varphi_{\rm zp}^{(n)}(a_n + a_n^\dagger) + \frac{1}{2}\omega_J t\right],\end{aligned} \tag{S27}$$

where we have neglected the gate voltage dependent term in the cavity mode coordinate part of the Hamiltonian and where $\varphi_{\rm zp}^{(n)}$ is the zero-point uncertainty of the cavity

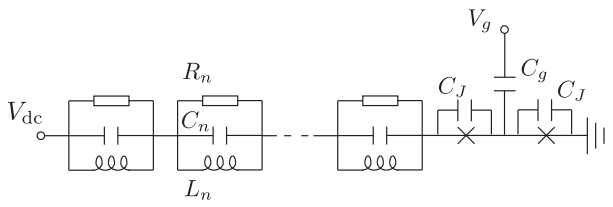

FIG. S6. Lumped element circuit model of the CPT-cavity system.

mode phase coordinate q_n:

$$\varphi_{\rm zp}^{(n)} = \sqrt{\frac{\pi\sqrt{L_n/C_n}}{4R_Q}} = \sqrt{\frac{Z_n}{4R_Q}}, \tag{S28}$$

with Z_n the cavity mode impedance. Restricting to the lowest, $n = 1$ cavity mode and truncating to a two-dimensional subspace involving linear combinations of only zero ($|0\rangle$) and one ($|1\rangle$) excess Cooper pairs on the island then yields the cCPT Hamiltonian (1) given in the main text.

Application of $P(E)$ theory

The low-temperature cotunneling current in a CPT coupled to an environment with impedance $Z(\omega)$ as predicted by $P(E)$ theory is given by[5,6] $I_{\rm cot} = 2e\Gamma_{\rm cot}$ where

$$\Gamma_{\rm cot} = \frac{\pi}{2\hbar}[E_J^{(1)}]^2 P(E) \tag{S29}$$

is the Cooper pair cotunneling rate and $E_J^{(1)} \approx 0.4E_J$. Here $P(E)$ is given by

$$P(E) = \frac{1}{2\pi\hbar}\int_{-\infty}^{\infty} dt\, e^{J(t)+iEt/\hbar} \tag{S30}$$

where $J(t)$ is the phase-phase correlation function given at zero temperature by[7]

$$J(t) = 2\int_0^\infty \frac{d\omega}{\omega}\frac{{\rm Re}Z_t(\omega)}{R_Q}(e^{-i\omega t}-1). \tag{S31}$$

Here $R_Q = h/4e^2$ is the resistance quantum and $Z_t(\omega)$ is the total impedance seen by the tunneling Cooper pairs. In our case, $Z_t(\omega)$ is the parallel combination of the CPT junction capacitance C_J and the parallel effective LCR resonance of the cavity (see Fig. S6). Since $C_J \ll C$, the junction capacitance has negligible influence on $Z_t(\omega)$, which is then approximately equal to the impedance $Z(\omega)$ of the resonator itself. We therefore have

$$Z_t(\omega) \approx Z(\omega) = \frac{1}{C}\frac{\omega}{i(\omega^2-\omega_0^2)+\omega\omega_0/Q}. \tag{S32}$$

Using $\omega_0 = (LC)^{-1/2}$, $Z_0 = \pi\sqrt{L/C}$ and $\varphi_{\rm zp}^2 = Z_0/4R_Q$, we can write (assuming a sharp resonance)

$$\frac{{\rm Re}Z(\omega)}{R_Q} = \frac{4\varphi_{\rm zp}^2\omega_0^2}{\pi Q}\frac{1}{4(\omega-\omega_0)^2+\omega_0^2/Q^2}. \tag{S33}$$

Substituting (S33) into (S31) and integrating gives the result

$$J(t) = -4\varphi_{\rm zp}^2 + 4\varphi_{\rm zp}^2 e^{-\omega_0|t|/2Q}e^{-i\omega_0 t} \tag{S34}$$

which, since $\varphi_{\rm zp}^2 \ll 1$, implies $|J(t)| \ll 1$. In evaluating the Fourier transform of $J(t)$ to find $P(E)$, we can perform a Taylor series expansion of $e^{J(t)}$. Doing so, and retaining only terms to second order in $\varphi_{\rm zp}^2$, we can obtain expressions for $P(E)$ in the vicinity of $E = \hbar\omega_0$ and $\hbar(2\omega_0)$. Making the substitutions $\kappa = \omega_0/Q$ and $\omega = E/\hbar$, we find

$$\Gamma_{\rm cot}(\omega\sim\omega_0) \approx \left(\frac{E_J^*\varphi_{\rm zp}}{\hbar}\right)^2 \frac{\kappa}{(\omega-\omega_0)^2+(\kappa/2)^2} \tag{S35}$$

where $E_J^* = E_J^{(1)}e^{-2\varphi_{\rm zp}^2} \approx 0.4E_J$, and

$$\Gamma_{\rm cot}(\omega\sim2\omega_0) \approx \left(\frac{E_J^*\varphi_{\rm zp}^2}{\hbar}\right)^2 \frac{4\kappa}{(\omega-2\omega_0)^2+(\kappa)^2}. \tag{S36}$$

These expressions, which are equivalent to previous results[8], give rise to maximum cotunneling rates

$$\Gamma_{\rm cot}^{(1)} = \left(\frac{4E_J^{*2}}{\hbar^2\kappa}\right)\varphi_{\rm zp}^2 \tag{S37}$$

and

$$\Gamma_{\rm cot}^{(2)} = \varphi_{\rm zp}^2\Gamma_{\rm cot}^{(1)}. \tag{S38}$$

For our parameters, $\Gamma_{\rm cot}^{(1)} \approx 1\times10^{12}$ s^{-1} and $\Gamma_{\rm cot}^{(2)} \approx 2\times10^9$ s^{-1}, both far greater than κ. The corresponding predicted currents are $I_{\rm cot}^{(1)} = 2e\Gamma_{\rm cot}^{(1)} \approx 0.4\ \mu$A for $\omega_J = \omega_0$ and $I_{\rm cot}^{(2)} = 2e\Gamma_{\rm cot}^{(2)} \approx 0.8$ nA $\omega_J = 2\omega_0$. Both are significantly larger than the measured values, the first almost unphysically so.

To find the predicted number $n_{\rm ph}$ of cavity photons for $\omega_J = \omega_0$, we substitute $\kappa = \omega_0/Q$ in (S37) and find

$$n_{\rm ph} = \frac{\Gamma_{\rm cot}^{(1)}}{\kappa} = 4\left(\frac{E_J^{*2}}{\hbar\omega_0}\right)^2 Q^2\varphi_{\rm zp}^2 \sim 4Q^2\varphi_{\rm zp}^2 \sim 10^5 \tag{S39}$$

as in the main text, because in our case $(E_J^*/\hbar\omega_0)^2$ is of order unity. Note that the theory also predicts $n_{\rm ph}$ at $\omega_J = 2\omega_0$ will be smaller by a factor of $2\varphi_{\rm zp}^2 \approx 3\times10^{-3}$ than at $\omega_J = \omega_0$, whereas in the experiment it is two times larger.

Finally, the theory predicts[8,9] an emisssion linewidth at $\omega_J = \omega_0$ and $2\omega_0$ of about the bare cavity linewidth $\kappa/2\pi \approx 1.5$MHz, as compared to the far smaller measured linewidths of 70 kHz and 350 kHz.

Quantum dynamics of the model system

In this Section we investigate the dynamics of the single-mode system within the charge state basis $|0\rangle$ and $|1\rangle$. Generically the dynamics of the system is described by a master equation of the form,

$$\dot{\rho} = -\frac{i}{\hbar}[H,\rho] + \mathcal{L}_N\rho + \mathcal{L}_n\rho, \tag{S40}$$

where H is given by (1), the terms $\mathcal{L}_N\rho$ and $\mathcal{L}_n\rho$ describe the effect of the environment on the island charge and cavity mode respectively.

We will not derive the dissipative parts of the master equation here, but instead take a phenomenological approach. We assume the simplest possible form for $\mathcal{L}_N\rho$, allowing transitions between charge states (for $\varepsilon > 0$),

$$\mathcal{L}_N\rho = \Gamma\left(\sigma_-\rho\sigma_+ - \frac{1}{2}\left\{\sigma_+\sigma_-,\rho\right\}\right), \tag{S41}$$

where Γ is the charge relaxation rate and $\sigma_+ = (\sigma_-)^\dagger = |1\rangle\langle 0|$, an approach which we expect to provide a reasonable description of the dissipative dynamics in the regime where $n_g \ll 1$. For the cavity mode we assume dissipation due to an oscillator bath at zero temperature and hence we have,

$$\mathcal{L}_n\rho = \frac{\omega_0}{Q}\left(a\rho a^\dagger - \frac{1}{2}\left\{a^\dagger a,\rho\right\}\right), \tag{S42}$$

where Q is the quality factor.

Semi-classical description

Given the master equation, Eq. (S40), we can write down equations of motion for the expectation values of the operators, a, σ_+ and σ_z,

$$\langle\dot{a}\rangle = -\left(i\omega_0 + \frac{1}{2Q}\right)\langle a\rangle - i\frac{E_J\varphi_{\rm zp}}{\hbar}\langle\sin[\varphi_{\rm zp}(a+a^\dagger) + \frac{1}{2}\omega_J t](\sigma_+ + \sigma_-)\rangle \tag{S43}$$

$$\langle\dot{\sigma}_+\rangle = \left(i\frac{2\varepsilon}{\hbar} - \Gamma\right)\langle\sigma_+\rangle + i\frac{E_J}{\hbar}\langle\cos[\varphi_{\rm zp}(a+a^\dagger) + \frac{1}{2}\omega_J t]\sigma_z\rangle \tag{S44}$$

$$\langle\dot{\sigma}_z\rangle = i\frac{2E_J}{\hbar}\langle\cos[\varphi_{\rm zp}(a+a^\dagger) + \frac{1}{2}\omega_J t](\sigma_+ - \sigma_-)\rangle - \Gamma(\langle\sigma_z\rangle + 1). \tag{S45}$$

We proceed by making a semi-classical approximation [10], treating expectation values of products of operators as products of expectation values. Adopting the notation $\alpha = \langle a\rangle$, $\sigma = \langle\sigma_+\rangle$, $z = \langle\sigma_z\rangle$, we obtain the following self-contained equations of motion for the system,

$$\dot{\alpha} = -\left(i\omega_0 + \frac{1}{2Q}\right)\alpha - i\frac{E_J\varphi_{\rm zp}}{\hbar}\sin[\varphi_{\rm zp}(\alpha+\alpha^*) + \frac{1}{2}\omega_J t](\sigma + \sigma^*) \tag{S46}$$

$$\dot{\sigma} = \left(i\frac{2\varepsilon}{\hbar} - \Gamma\right)\sigma + i\frac{E_J}{\hbar}\cos[\varphi_{\rm zp}(\alpha+\alpha^*) + \frac{1}{2}\omega_J t]z \tag{S47}$$

$$\dot{z} = i\frac{2E_J}{\hbar}\cos[\varphi_{\rm zp}(\alpha+\alpha^*) + \frac{1}{2}\omega_J t](\sigma - \sigma^*) - \Gamma(z+1). \tag{S48}$$

Origin of the resonances

The sequential tunneling resonances shown schematically in Fig. 1e (left panel) involve a two step cycle of processes which transfer Cooper pairs across one junction at a time. In the first step, a Cooper pair tunnels across one of the junctions taking the island from the lower to the higher energy charge state whilst at the same time a photon is emitted into the cavity. This process occurs when the voltage lost by the Cooper pair tunneling across the junction balances the change in charging energy and the cost of photon production, $\frac{1}{2}\hbar\omega_J = 2|\varepsilon| + \hbar\omega_0$, which defines the diagonal resonance lines. After this first step, the island is in the higher energy charge state so the system can return to the lower charge state in the second step via the tunneling of a Cooper pair across the other junction (with the extra energy being dissipated not in the cavity mode, but in other environmental degrees of freedom, i.e. through the $\mathcal{L}_N\rho$ terms in the master equation).

The simplest way of understanding the locations of the cotunneling resonances shown in Fig. 1e (right panel) is in terms of matching between the voltage energy lost by

a Cooper pair traversing both CPT junctions and the energy required to create k photons, $2eV_{\rm CPT} = \hbar\omega_J = k\hbar\omega_0$. As one would expect, the cotunneling resonances appear in the semi-classical equations. Their locations can be determined (though not what the corresponding steady states are) by assuming that the occupation of the cavity is small (i.e. $\alpha \ll 1$) so that the effect of the cavity on the dynamics of the CPT island charge can be neglected. Dropping the dependence on α in Eqs. (S47) and (S48), we are left with a pair of equations which describes a two-level system subject to both a harmonic drive and damping,

$$\dot{\sigma} = \left(i\frac{2\varepsilon}{\hbar} - \Gamma\right)\sigma + i\frac{E_J}{\hbar}\cos(\omega_d t)z \tag{S49}$$

$$\dot{z} = i\frac{2E_J}{\hbar}\cos(\omega_d t)(\sigma - \sigma^*) - \Gamma(z+1), \tag{S50}$$

where for convenience we have introduced the single-junction driving frequency $\omega_d = \frac{1}{2}\omega_J$. The long time behavior of the CPT island charge will be a periodic function of ω_d. For reasons of symmetry [11], $\sigma(t)$ contains only odd harmonics and hence can be expressed as the Fourier series

$$\sigma(t) = \sum_n{}' c_n \mathrm{e}^{in\omega_d t}, \tag{S51}$$

with the prime indicating that the sum runs over odd integers.

Defining $\tilde{\alpha} = \alpha \mathrm{e}^{i\omega_0 t}$, and substituting the Fourier series (S51) for $\sigma(t)$, into the Eq. (S46) we find

$$\dot{\tilde{\alpha}} = -\frac{\tilde{\alpha}}{2Q} - i\frac{E_J\varphi_{\rm zp}}{\hbar}\mathrm{e}^{i\omega_0 t}\sum_n{}'\left(c_n\mathrm{e}^{in\omega_d t} + c_n^*\mathrm{e}^{-in\omega_d t}\right) \times \sin\left[\varphi_{\rm zp}\left(\tilde{\alpha}\mathrm{e}^{-i\omega_0 t} + \tilde{\alpha}^*\mathrm{e}^{i\omega_0 t}\right) + \omega_d t\right]. \tag{S52}$$

Resonances occur whenever the damping term is matched by another term which has no explicit time dependence. Expanding out the sinusoidal term, we see that there are exponentials with all integer powers of ω_0, but only even powers of ω_d, hence the most general resonance condition is $k\omega_0 = 2p\omega_d = p\omega_J$, corresponding to k photons being produced by the cotunneling of p Cooper pairs. In addition there is a time independent contribution which is present for any combination of ω_d and ω_0 (it is generated by terms in the expansion of the sine that are proportional to $\mathrm{e}^{-i\omega_0 t}$). However, this term is dispersive leading to a frequency shift in the cavity mode and it does not affect the energy.

At the one photon resonance where $\omega_J = 2\omega_d = \omega_0$, oscillations of $\sigma(t)$ at frequency ω_d act to upconvert the single-junction drive oscillations (also at ω_d) to produce oscillations at frequency $\omega_J = 2\omega_d$ which are resonant with the cavity mode. Expanding Eq. (S52) to linear order in $\tilde{\alpha}$ and retaining only terms without explicit time dependence we find,

$$\dot{\tilde{\alpha}} = -\frac{\tilde{\alpha}}{2Q} + \frac{E_J\varphi_{\rm zp}}{2\hbar}\beta_0 - i\frac{E_J\varphi_{\rm zp}^2}{2\hbar}\left(\beta_1\tilde{\alpha} + \beta_2\tilde{\alpha}^*\right) \tag{S53}$$

where the β coefficients depend on the Fourier components,

$$\beta_0 = c_{-1} + c_1^* - c_{-3} - c_3^* \tag{S54}$$

$$\beta_1 = c_{-1} + c_1 + c_{-1}^* + c_1^* \tag{S55}$$

$$\beta_2 = c_{-3} + c_3^* + c_{-5} + c_5^*. \tag{S56}$$

The β_0 and β_2 terms in Eq. (S53) arise because of the resonance condition $\omega_d = \omega_0/2$ and lead to changes in the energy of the mode, with the β_0 term acting like a linear drive. The β_1 term is independent of the specific choice of ω_d and generates only a frequency shift (since β_1 is real).

A similar picture emerges at the two photon resonance where $\omega_J = 2\omega_d = 2\omega_0$ where an expansion leads to

$$\dot{\tilde{\alpha}} = -\frac{\tilde{\alpha}}{2Q} - i\frac{E_J\varphi_{\rm zp}^2}{2\hbar}\left(\beta_1\tilde{\alpha} + \beta_3\tilde{\alpha}^*\right), \tag{S57}$$

where here $\beta_3 = c_{-3} + c_3^* + c_{-1} + c_1^*$. The β_1 term again leads to a frequency shift while the β_2 term, which arises because of resonance condition ($\omega_d = \omega_0$), generates changes in the energy of the mode.

The simple resonance condition suggests that, in a crude sense, the CPT can be thought of as acting like a single effective Josephson junction at the cotunneling resonances as there is no explicit energy matching condition involving the internal state of the island (and hence the gate voltage), though the behavior of the system *does* depend on n_g implicitly through the dynamics of σ. However, at points where the two island charge states are degenerate (i.e. $n_g = 1$ and hence $\varepsilon = 0$) the driven oscillations in σ described by Eqs. (S47) and (S48) become entirely imaginary leading to a decoupling from the cavity (since it is the combination $\sigma + \sigma^*$ which appears in Eq. S46 for α), a feature which should not depend on the details of the dissipative terms. In Eqs. (S53) and (S57) the β coefficients vanish for a pure imaginary σ since in that case $c_n = -c_{-n}^*$. Thus both the driving of the cavity and the frequency shift terms generated by the interaction with the CPT should shut off at the charge degeneracy point. This provides an explanation for the loss of cavity output seen around $n_g = \pm 1$ in the experiment.

Dynamics at the cotunneling resonances

The level of cavity excitation predicted by the model can be obtained by integrating Eqs. (S46)-(S48) and calculating the long time average of $|\alpha|^2$ which is equivalent to the average number of cavity photons. Figure S7 shows an example of the behavior as a function of $\varphi_{\rm zp}$

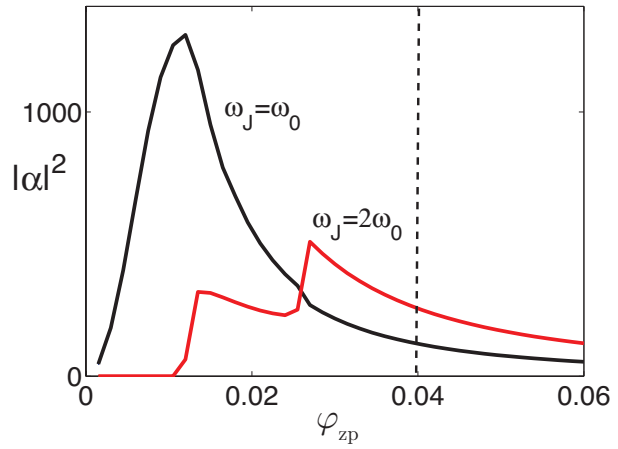

FIG. S7. Average cavity energy calculated semi-classically, $|\alpha|^2$, in the long time limit at the one and two photon resonances as a function of $\varphi_{\rm zp}$. We use the parameter values from the experiment $Q = 3500$, $E_J/\hbar\omega_0 = 3.2$, $4E_c/\hbar\omega_0 = 6.6$, $n_g = 0$ and choose $\Gamma/\omega_0 = 0.02$.

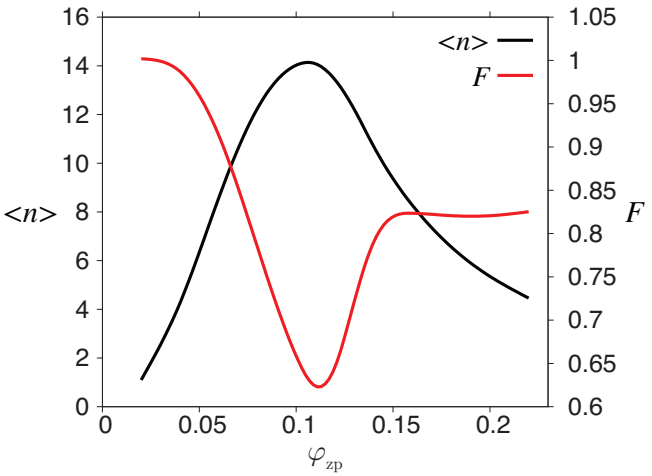

FIG. S8. Average cavity occupation, $\langle n\rangle$, and Fano factor, F, as a function of $\varphi_{\rm zp}$ for $\omega_J = \omega_0$ in the limit of long times. Here $E_J/\hbar\omega_0 = 2$, $\varepsilon/\hbar\omega_0 = 2.5$, $Q = 75$ and $\Gamma/\omega_0 = 0.2$.

at the one and two photon resonances. For the one photon resonance there is a smooth increase in energy as a function of $\varphi_{\rm zp}$ followed by a peak and then a decaying region. The two photon resonance grows abruptly in two stages before also decaying in a similar way to the one photon case. For the experimental value $\varphi_{\rm zp} = 0.04$ we obtain photon numbers of 122 for $\omega_J = \omega_0$ and 256 for $\omega_J = 2\omega_0$, which are very similar in magnitude to the results described in the main text.

Numerical integration of the master equation (S40) allows us to examine the quantum fluctuations in the system [12], although we have not explored the regime probed in the experiment as the photon numbers involved are too high (instead larger values of $\varphi_{\rm zp}$ are combined with much lower values of Q). Such calculations certainly suggest that amplitude-squeezing ($F < 1$) is a generic property of the system. Figure S8 shows an example of the kind of results which can be obtained in this way for $\omega_J = \omega_0$. The average energy behaves in the same general way as that obtained from the semi-classical equations for the experimentally relevant parameters (shown in Fig. S7). Amplitude-squeezing occurs over the whole range of $\varphi_{\rm zp}$ studied.

Further evidence of the system's very general tendency to display amplitude-squeezing comes from analysis of a model describing an analogous one junction system [13]. In this system Fano factors less than unity are found generically for a very broad range of parameters at the one and two photon resonances, including the regime where $Q \geq 1000$ and $\varphi_{\rm zp} \simeq 0.04$. Finally, we point out that the lowest Fano factors are usually associated with systems where there is an interaction between a harmonic mode and a two-level system, a prominent example being the trapping states of the micromaser [14] (where almost pure Fock states can in principle be generated). Indeed, recent work by Marthaler et al. [15] predicted the existence of trapping states in a model CPT-cavity system for processes where changes in island charge state are associated with photon emission (closely related to the sequential resonances observed in the experiment).

1. Chen, F., Sirois, A. J., Simmonds, R. W. & Rimberg, A. J. Introduction of a dc bias into a high-Q superconducting microwave cavity. *Appl. Phys. Lett.* **98**, 132509 (2011).
2. Dolan, G. J. Offset masks for lift-off photoprocessing. *Appl. Phys. Lett.* **31**, 337 (1977).
3. Xue, W. W. *et al.* Measurement of quantum noise in a single electron transistor near the quantum limit. *Nature Phys.* **5**, 660–664 (2009).
4. Aassime, A., Gunnarsson, D., Bladh, K., Delsing, P. & Schoelkopf, R. Radio-frequency single-electron transistor: Toward the shot noise limit. *Appl. Phys. Lett.* **79**, 4031–4033 (2001).
5. Zorin, A. B. Quantum-limited electrometer based on single Cooper pair tunneling. *Phys. Rev. Lett.* **76**, 4408 (1996).
6. Lotkhov, S. V., Bogoslovsky, S. A., Zorin, A. B. & Niemeyer, J. Cooper pair cotunneling in single charge transistors with dissipative electromagnetic environment. *Phys. Rev. Lett.* **91**, 197002 (2003).
7. Ingold, G.-L., Grabert, H. & Eberhardt, U. Cooper-pair current through ultrasmall Josephson junctions. *Phys. Rev. B* **50**, 395–402 (1994).
8. Hofheinz, M. *et al.* Bright side of the Coulomb blockade. *Phys. Rev. Lett.* **106**, 217005 (2011).
9. Ingold, G.-L. & Grabert, H. Finite-temperature current-voltage characteristics of ultrasmall tunnel junctions. *Europhys. Lett.* **14**, 371–376 (1991).
10. Walls, D. F. & Milburn, G. J. *Quantum Optics* (Springer, Berlin, 2008).
11. Grifoni, M. & Hänggi, P. Driven quantum tunneling.

Phys. Reports **204**, 229–354 (1998).

12. Johansson, J. R., Nation, P. & Nori, F. QuTiP: An open-source Python framework for the dynamics of open quantum systems. *Comp. Phys. Comms.* **183**, 1760–1772 (2012).
13. Armour, A. D., Blencowe, M. P., Brahimi, E. & Rimberg, A. J. Universal quantum fluctuations of a cavity mode driven by a Josephson junction. *Phys. Rev. Lett.* **111**, 247001 (2013).
14. Haroche, S. & Raimond, J.-M. *Exploring the Quantum* (Oxford University Press, Oxford, 2006).
15. Marthaler, M., Leppäkangas, J. & Cole, J. H. Lasing, trapping states, and multistability in a circuit quantum electrodynamical analog of a single-atom injection maser. *Phys. Rev. B* **83**, 180505(R) (2011).